Acta Materialia 213 (2021) 116934

Contents lists available at ScienceDirect

Acta Materialia

journal homepage: www.elsevier.com/locate/actamat

Full length article

An integrated experimental and computational investigation of defect and microstructural effects on thermal transport in thorium dioxide

Cody A. Dennett[a,1,*], W. Ryan Deskins[b,1], Marat Khafizov[c], Zilong Hua[a], Amey Khanolkar[a], Kaustubh Bawane[d], Lyuwen Fu[e], J. Matthew Mann[f], Chris A. Marianetti[e], Lingfeng He[d], David H. Hurley[a], Anter El-Azab[b]

[a] Materials Science and Engineering Department, Idaho National Laboratory, Idaho Falls, ID 83415, USA
[b] School of Materials Engineering, Purdue University, West Lafayette, IN 47907, USA
[c] Department of Mechanical and Aerospace Engineering, The Ohio State University, Columbus, OH 43210, USA
[d] Advanced Characterization Department, Idaho National Laboratory, Idaho Falls, ID 83415, USA
[e] Department of Applied Physics and Applied Mathematics, Columbia University, New York, New York 10027, USA
[f] Air Force Research Laboratory, Sensors Directorate, Wright-Patterson AFB, OH 45433, USA

ARTICLE INFO

Article history:
Received 5 January 2021
Revised 7 April 2021
Accepted 22 April 2021
Available online 26 April 2021

Keywords:
Thermal conductivity
Thorium dioxide
Defects
Boltzmann transport equation

ABSTRACT

Advanced nuclear reactor concepts aim to use fuels that must withstand unprecedented temperature and radiation extremes. In these fuels, thermal energy transport under irradiation is directly related to fuel longevity, reactor safety, and is arguably one of the most important performance metrics. Here we provide a comprehensive, first-principles-informed treatment of phonon mediated thermal transport in a defect-bearing actinide oxide with direct comparison to experimental measurements. Pristine and proton irradiated thorium dioxide was chosen as a model system to treat the complexity of thermal transport in the presence of lattice defects. A thermal transport model is implemented using the linearized Boltzmann transport equation (LBTE) with input from first principles calculations and defect evolution models. Density functional theory is used to calculate phonon dispersion in thorium dioxide and used as an input to calculate both intrinsic and extrinsic, defect-induced relaxation times. In addition, a defect evolution model is benchmarked using microstructure characterization of as-irradiated thorium dioxide using a combination of electron microscopy and optical spectroscopy. The output of the LBTE is compared directly to mesoscopic measurements of thermal conductivity on length scales commensurate with defect accumulation. Parametric measurements of conductivity with irradiation dose and temperature suggest a saturation in the reduction of thermal conductivity with increasing defect generation, which is partially captured in our defect evolution model and LBTE framework. This comprehensive, atomistic- to meso-scale treatment provides the necessary basis to investigate thermal transport under irradiation in more complex systems that exhibit strong electron correlation.

1. Introduction

The transport of thermal energy underlies the physics basis for electrical generation or conversion in the majority of energy systems utilized worldwide. Of solid-state materials, ceramic oxides form the technical basis for a large portion of net electricity generation, as nuclear fuels, and are key fuel cell materials. In nuclear ceramics, particularly uranium dioxide (UO_2), significant evolution of microstructure and material properties takes place over an operational lifetime, often drastically modifying thermal transport. However, a complete atomistic-to-fuel scale understanding of thermal transport in actinide oxides remains a grand challenge due to complexities associated with accurately treating electron correlation in UO_2 [1]. To develop a comprehensive toolkit for thermal transport in fuel materials, the most practical pathway is to first analyze a surrogate material free of electron correlation effects. In the case of UO_2, a suitable choice for such a surrogate is thorium dioxide (ThO_2). ThO_2 is a fluorite oxide isostructural with UO_2 with similar cation to anion mass ratio. ThO_2 has also been

* Corresponding author.
E-mail addresses: cody.dennett@inl.gov (C.A. Dennett), aelazab@purdue.edu (A. El-Azab).
[1] These authors contributed equally to this work

https://doi.org/10.1016/j.actamat.2021.116934

proposed, either by itself or as a mixed actinide oxide $U_xTh_{1-x}O_2$, as an alternative nuclear fuel due to desirable characteristics such as high melting temperature, higher thermal conductivity, and proliferation resistance [2–4].

In operation, a variety of extreme environmental factors including high levels of radiation, the formation of solid and gaseous fission-product species, and high temperatures all serve to induce microstructure evolution and property degradation in actinide oxide fuel systems [5]. These factors will induce a variety of effects (point and extended defect formation, grain restructuring, gas bubble agglomeration) which all serve to limit the mean free path of phonons, the heat carries in oxide fuels [6–8]. For UO_2, reduced-order performance models treating these effects have been constructed through the collection of large experimental data sets over decades [9,10]. However, a gap currently exists between the first principles understanding of thermal transport in these systems and the desire for reduced-order analysis suitable for the development of advanced fuels (arbitrary chemical compositions and microstructures). To most efficiently design and implement advanced fuel concepts, a first-principles-informed understanding of thermal transport, and how transport is affected by defects, must be generated by a combination of controlled experiments and modeling. Generating such a physics basis for ThO_2 serves as the first step towards this understanding.

While several research groups have reported first principles treatments of thermal transport in perfect ThO_2 single crystals [11–13], only very few first principles studies of thermal transport in defect-bearing ThO_2 have been conducted recently [14]. Most thermal transport modeling work has either involved DFT coupled with a simplified Slack model to predict thermal transport in perfect crystals [15] or MD simulation using empirical interatomic potentials [8,16]. The introduction of defects into ThO_2 either through synthesis or irradiation exposure increases the difficulty of predicting thermal conductivity. For example, the sintered ceramics pellets which are most commonly studied have retained porosity and grain boundaries that significantly impact measured values of thermal conductivity compared to values for perfect crystals [17,18]. This challenge has led some authors to re-scale experimental measurements to fixed values of theoretical density using empirical models to compare with simulation outputs [17]. Even in these cases, calculated conductivities are routinely higher than those measured in experiment. Initial efforts to measure high-quality single crystals of ThO_2 using either bulk [18] or mesoscale-meoso [6] transport methods have shown that eliminating defects produced during synthesis provides a straightforward path to create a consistent experimental and modeling framework. A defect-free baseline material can then be used to systematically study the influence of defects on thermal transport by introducing small-scale lattice defects (e.g. point defects, dislocation loops) in a controlled fashion using ion irradiation.

However, a significant challenge in studying the effects of lattice defects on thermal transport in these ion irradiated materials is the outsized role played by defects on the smallest scales which cannot be fully quantified through electron microscopy [6,19]. Although recent progress has been made with incorporating the impact of phonon scattering by these small-scale defects in computational transport models of ThO_2 [16,20], experimental methods capable of characterizing these defect populations are not widely available. A notable recent example of progress in this area is that of Khafizov and coworkers, who used a combination of X-ray diffraction (XRD) and thermal transport measurements to reveal point defect densities in ion irradiated UO_2 [21]. Although bespoke solutions have been pursued for specific material systems, a framework for reliably determining these defect concentrations which shows agreement between experiments and simulations has yet to be achieved.

With an understanding of current challenges and gaps in phonon-mediated thermal transport in actinide oxides in the presence of lattice defects, this work presents a first-principles-informed computational and experimental investigation of thermal transport in defected ThO_2. Here, we expose high-quality single crystals of ThO_2 to 2 MeV proton (H^+ ion) irradiation to generate a microscale, defect-bearing region. Exposures are conducted in two different temperature regimes (20 °C and 600 °C) to vary the character of the resulting defect population in a controlled manner, promoting dislocation loop formation at high temperatures and constraining defect sizes at room temperature.

Following irradiation exposure, a comprehensive experimental and computational investigation is undertaken (1) to quantify the character and density of defects formed at these different temperatures; (2) to directly measure the defect-affected thermal transport properties of the ion-modified region; (3) to use a combination of spectroscopy and defect evolution modeling to infer populations of defects which cannot be quantified directly; and (4) to use the measured and inferred defect characteristics as inputs into a linearized Boltzmann transport equation (LBTE) framework to predict thermal transport and compare with our experimentally-measured quantities. In doing so, we utilize updated phonon band structures for ThO_2 calculated from first principles using density functional theory (DFT) with LBTE to calculate modified phonon scattering rates and to investigate the reduction in conductivity as a result of defects. Importantly, the thermal conductivity at low temperatures is measured for a subset of the as-irradiated crystals to study a regime where different lattice defects affect phonon scattering with different relative strengths. Together, this combined experimental, analytical, and computational treatment provides a comprehensive insight into the accumulation of lattice defects in ThO_2 and their effects on thermal transport.

2. Methodology

2.1. Experimental

The hydrothermal synthesis technique was used to grow {001} oriented single crystals of ThO_2 for this study. A detailed description of this method and discussion of the resulting crystal purity can be found elsewhere [6,18]. Six ThO_2 crystals were mounted to copper blocks and exposed to 2 MeV protons (H^+ ions) at 20 °C (3 samples) and 600 °C (3 samples) using the 3 MV tandem pellatron accelerator at Texas A&M University. Samples were exposed to a rastered ion beam with a 20% overscan of each crystal face to ensure a uniform dose across the sample surface with a flux of 1.8×10^{13} ions/cm^{2}s. Temperature monitoring was carried out during irradiation by a thermocouple press-fit to the copper mounting block. This feedback was used to ensure no significant ion beam heating occurred at room temperature and was used to actively control the sample temperature for 600 °C exposures. The depth distribution of damage induced by the proton beam was calculated using the Stopping Range of Ions in Matter (SRIM) code in the full cascade mode using the room temperature theoretical density of ThO_2 and displacement energies of $E_d = 48.5$ eV and 17.5 eV for thorium and oxygen respectively [22–24]. Given the peak displacement damage at 24 μm, as seen in Fig. 1, a 'plateau' damage region was identified consisting of an 18 μm surface layer of the exposed samples. Averaging over this plateau region, 20 °C samples were exposed to doses of 0.016, 0.079 and 0.16 displacements per atom (dpa) and 600 °C samples were exposed to doses of 0.16, 0.47, and 0.79 dpa. A summary of irradiation conditions is shown in Table 1.

To investigate anion sublattice vacancy-type defects retained following irradiation, optical ellipsometry measurements were performed on 'HT' series thoria crystals irradiated at 600 °C. Optical constants and dielectric properties of the pristine and irradiated

Table 1
Summary of applied irradiation conditions including sample ID, irradiation temperature, ion fluence, and total dose received over the 18 μm 'plateau' region in dpa.

Sample ID	Irradiation Temperature	Ion Fluence $\left[\text{ions/cm}^2\right]$	Average Dose over 18 μm [dpa]
RT1	20 °C	1.727×10^{17}	0.016
RT2	20 °C	8.635×10^{17}	0.079
RT3	20 °C	1.727×10^{18}	0.16
HT1	600 °C	1.727×10^{18}	0.16
HT2	600 °C	5.181×10^{18}	0.47
HT3	600 °C	8.635×10^{18}	0.79

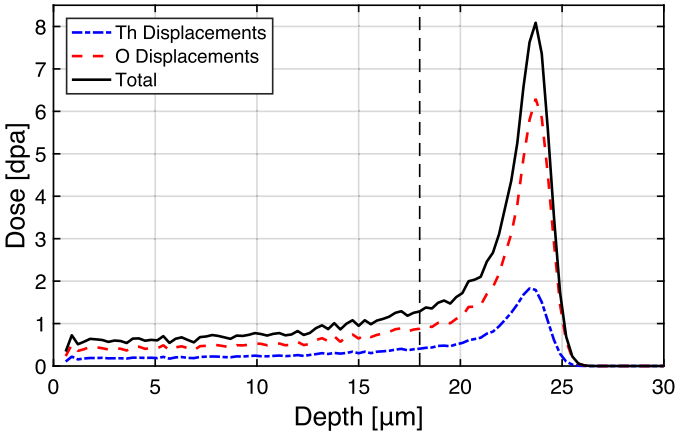

Fig. 1. Applied dose profile for 2 MeV H^+ in ThO_2 showing Th and O sublattice displacements as well as total dose for highest applied fluence, 8.635×10^{18} ions/cm^2. The dashed vertical line at 18 μm indicates the identified plateau region over which dose values are averaged.

thoria crystals were measured using a rotating compensator ellipsometer (M-2000, J.A. Woollam Company) in the spectral range of 350 nm to 1000 nm (1.24 eV to 3.5 eV). Spectroscopic ellipsometry data were acquired at a fixed angle of incidence of 60°.

Thermal diffusivity as a function of temperature of the plateau damage layer of two irradiated ThO_2 samples (HT1 and HT2, both irradiated at 600 °C) and one pristine sample was extracted using the spatial-domain thermoreflectance (SDTR) technique. This sample subset was selected to interrogate both point defect and dislocation loop phonon scattering and based on geometric sample constraints. In SDTR, a transient local temperature variation is induced by using an intensity-modulated CW laser with a wavelength of 660 nm, and detected by using a constant-intensity CW laser with a wavelength of 532 nm through the thermoreflectance effect. A 50× objective lens is used to focus the laser beams to improve the spatial resolution. The radius of both laser spots at the sample surface was approximately 2 μm for these measurements, with an optical power of ∼1 mW and ∼0.3 mW for the heating and probe lasers, respectively.

During SDTR measurements, the heating laser spot is scanned across the probe laser in one dimension by ∼10 μm in either direction. The reflected probe laser beam is captured by a photodetector and its phase difference from the heating source is recorded with respect to the scan distance using a lock-in amplifier. In order to enhance the thermoreflectance effect, and thereby improve the signal-to-noise ratio, a gold film with a thickness of ∼27 nm was deposited on the surface of all samples. The thermal diffusivity of the sample is extracted by comparing this phase profile with one generated through a continuum thermal wave model. The details of the measurement system and the 3D thermal wave model used can be found elsewhere [25–27]. The influence of the deposited film layer on heat conduction is considered in the model, with its thermal conductivity at room temperature measured from a reference BK7 sample that was simultaneously coated with the ThO_2 samples. In extracting low-temperature thermal properties, the temperature dependence of gold thermal conductivity from Mason and coworkers for continuously-deposited films was parametrized and used such that all assumed material properties are consistent with the measurement temperature [28]. It is worth noting that the analytical model used in this work is a 3D transport model, compared with a simplified far-field model used in an initial investigation of a subset of these ThO_2 samples [6]. That simplified model relies on assumptions for the relative conductivities of the gold transducer film and crystal substrate which do not hold as the conductivity of pristine ThO_2 increases at low temperatures [29], necessitating the more sophisticated approach used here.

Low-temperature thermal transport measurements were conducted below 300 K to discriminate contributions to phonon scattering from defects of different types; above room temperature, an increased contribution from 3-phonon processes makes this defect discrimination more challenging [20]. To do so, ThO_2 samples were liquid-nitrogen cooled in an optical cryostat (Cryo Industries model XEM). In order to prevent ice condensation on the sample surface at low temperatures, the cryostat chamber was cyclically purged using ultrahigh purity nitrogen and then continually pumped to pressures below 1 mTorr during measurements. Measurements were performed from room temperature (297 K) to 77 K using a decrement of 25 K. An integrated electronic heater was used to maintain the target temperature, which is controlled by a feedback loop with a thermal sensor embedded into the copper cold head. In order to improve the temperature measurement accuracy, the temperature recorded by the thermal sensor was calibrated by two other approaches. The first is through an embedded thermocouple on the copper cold head surface, 1 cm away from the sample of interest, and the second is from a reference calcium fluoride (CaF_2) sample. The thermal diffusivity of CaF_2 is strongly related to temperature from 297 K to 77 K and thus can be used to estimate the actual temperature at the sample holder [30]. After calibration, the estimated temperature uncertainty using this apparatus is less than 3 K in the entire temperature region, including laser heating effects.

Following mesoscopic property measurements, cross sectional samples perpendicular to as-irradiated crystal surfaces were prepared using an FEI 3D Quanta focused ion beam (FIB) system. The samples were thinned to a final thickness of roughly 30–60 nm using 30 keV Ga ions and the final cleaning was conducted using 5 keV Ga ions. Lamella were extracted from the irradiated surface to ∼10 μm below and defect analysis was carried out in a region ∼2 μm below the surface, within the identified plateau region [6]. Comparisons between pristine and as-irradiated ThO_2 lamella show no indication of any FIB-induced damage in the final lamella. An FEI Titan Themis 200 transmission electron microscope (TEM) was used to characterize the defects in proton-irradiated samples. Bright-field (BF) TEM imaging was used to observe any dislocation loops formed in irradiated samples. Measurements of dislocation loop size and density were conducted manually from BF images. Electron energy loss spectroscopy (EELS) was used to

determine the thickness of FIB lamella using a known electron inelastic mean free path in ThO_2 [31]. Initial TEM characterization on this set of samples was reported in a previous work [6], and revealed that ThO_2 samples exposed at 20 °C did not show evidence of large-scale defect agglomeration on length scales >1 nm. As such, only micrographs of crystals exposed at 600 °C will be discussed in detail.

2.2. Computational

The phonon band structure of ThO_2 was calculated using DFT in conjunction with three different exchange-correlation functionals: the Local Density Approximation (LDA) [32], the Generalized Gradient Approximation (GGA, PW91) [33], and the Strongly Constrained and Appropriately Normed (SCAN) functional [34]. Calculations were performed using the Projector Augmented Wave (PAW) method [35,36], as implemented in the Vienna *Ab-initio* Simulation Package (VASP) [37–40]. A plane wave basis with a kinetic energy cutoff of 800 eV was employed with a Γ-centered k-point mesh of 20 × 20×20. The crystal structure was relaxed, yielding lattice parameters in the conventional cubic cell of 5.529 Å, 5.620 Å, and 5.592 Å for LDA, GGA, and SCAN, respectively. These values, particularly from SCAN, compare well with the experimental lattice parameter of 5.5970 Å from synchrotron XRD [41]. In order to include LO-TO splitting, we computed the dielectric constants and Born effective charges (in a.u.) and obtained diagonal elements of $\epsilon = 4.8790$, $Z^*_{Th} = 5.4097$, and $Z^*_O = -2.7031$ for LDA; $\epsilon = 4.7917$, $Z^*_{Th} = 5.3941$, and $Z^*_O = -2.6973$ for GGA; $\epsilon = 4.4819$, $Z^*_{Th} = 5.3166$, and $Z^*_O = -2.6737$ for SCAN.

Phonon calculations were performed using the lone irreducible derivative approach [42], extracting all irreducible derivatives within a 4×4×4 (multiplicity 64, 192 atoms) supercell but only requiring supercells up to multiplicity 4 (12 atoms) in doing so. Central finite difference calculations for each irreducible derivative are computed for a range of displacements, instead of a single value, and the results are then extrapolated to zero discretization. Fourier interpolation was then used to interpolate the phonons along high symmetry directions [42,43], and the LO-TO splitting was incorporated using the approach that is typically employed in conjunction with density functional perturbation theory [43].

The phonon dispersion of ThO_2 has previously been measured using inelastic neutron scattering by Clausen et. al (T=293K) [44], and more recently by Bryan et. al (T=300K) [45]. It has also been computed using DFT in numerous different studies [14,46–53]. However, we believe this to be the first implementation of the SCAN functional to calculate phonon dispersion in ThO_2. Fig. 2 provides a direct comparison between LDA, GGA, SCAN, and experiment. All three DFT functionals are in reasonable agreement with experiment. LDA and SCAN are very similar, only showing minor differences at intermediate energies. The GGA values are noticeably softer except at the lowest energies. Overall, LDA and SCAN appear to be slightly more favorable over GGA as compared to experiment. Values calculated using SCAN will be used in the remainder of this work.

To compute the conductivity of defected ThO_2, we adopt the LBTE framework for phonons outlined by Deskins and coworkers [20], which will briefly be summarized here. The interaction of phonons with other phonons in the system can be characterized by a relaxation time τ_{qs} defined as the average time between consecutive scattering events. The simplest method for estimating the relaxation time of a phonon with wavenumber q and vibrational mode s is the single-mode relaxation time approximation (SMRT) which assumes that all other phonon modes are in thermal equilibrium. For defect- and impurity-free crystals, the relaxation time is dominated by intrinsic 3-phonon processes, τ_{3ph} [20,54,55].

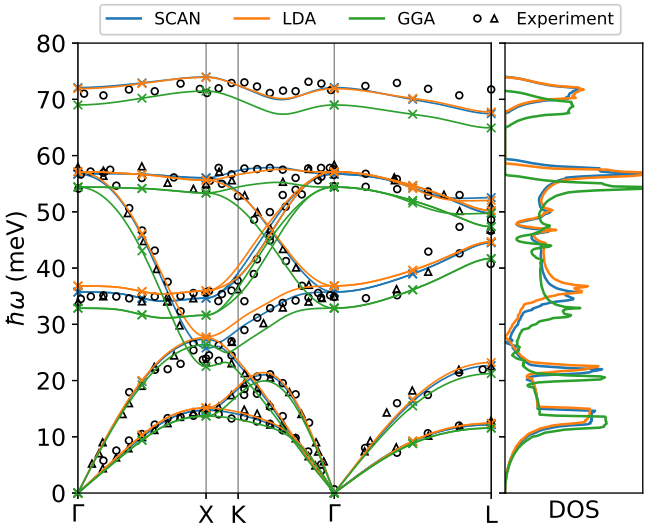

Fig. 2. (Left panel) Phonon dispersion of ThO_2 computed using DFT with various exchange-correlation functionals (LDA, GGA, SCAN) and measured using inelastic neutron scattering (circles [45] and triangles [44]). Colored points are the computed phonons, while the colored lines are Fourier interpolation. (Right panel) The phonon density of states.

The solution of the LBTE for phonons within the SMRT [54] yields an expression for lattice thermal conductivity, k, consistent with the kinetic theory result:

$$k = \sum_{qs} \frac{1}{3} c_{qs} \tau_{qs} \left(\mathbf{v}_g^{qs} \cdot \mathbf{v}_g^{qs} \right) = \frac{1}{3} \sum_{qs} c_{qs} \tau_{qs} \left| \mathbf{v}_g^{qs} \right|^2 \tag{1}$$

where $\mathbf{v}_g^{qs}$ is the phonon group velocity, and c_{qs} is the mode-specific, harmonic, lattice specific heat defined as

$$c_{qs} = \left(\frac{\hbar \omega_{qs}}{k_B T} \right)^2 \frac{k_B \exp\left(\hbar \omega_{qs} / k_B T\right)}{\left[\exp\left(\hbar \omega_{qs} / k_B T\right) - 1\right]^2}. \tag{2}$$

In the present work, this form for thermal conductivity was implemented in conjunction with the SMRT expression for intrinsic 3-phonon scattering processes [20,54] as

$$\begin{aligned} \tau_{qs}^{-1}\big|_{3ph} = \frac{\pi \hbar \gamma^2}{\rho N_0 \Omega_0 \left[v_p^{qs}\right]^2} \sum_{q's'q''s''} \omega_{qs} \omega_{q's'} \omega_{q''s''} \\ \times \left[\frac{\bar{n}_{q's'} \left(\bar{n}_{q''s''} + 1 \right)}{\bar{n}_{qs} + 1} \delta\left(\omega_{qs} + \omega_{q's'} - \omega_{q''s''} \right) \delta_{q+q'-q'',G} \right. \\ \left. + \frac{1}{2} \frac{\bar{n}_{q's'} \bar{n}_{q''s''}}{\bar{n}_{qs}} \delta\left(\omega_{qs} - \omega_{q's'} - \omega_{q''s''} \right) \delta_{q-q'-q'',G} \right], \end{aligned} \tag{3}$$

where Ω_0 is the primitive unit cell volume, N_0 is the total number of primitive unit cells, ρ is the mass density, γ is the macroscopic Grüneisen parameter (taken as 2.0 [47]), v_p^{qs} is the phonon phase velocity, and $\bar{n}_{qs}$ is the equilibrium phonon distribution given by Bose-Einstein statistics. The conservation of energy and crystal momentum are enforced by the Dirac delta function, $\delta\left(\omega_{qs} \pm \omega_{q's'} - \omega_{q''s''}\right)$, and the Kronecker delta, $\delta_{q\pm q'-q'',G}$, respectively [20]. Here, G is a recriprocal lattice vector, which denotes normal ($G = 0$) and Umklapp scattering processes. In implementing Eq. 1, we have restricted our consideration of phonon scattering to Umklapp processes, as normal processes do not directly influence thermal resistivity [55].

To facilitate the calculation of phonon-phonon scattering rates, lattice specific heat, and thermal conductivity, a Brillouin zone summation of the desired quantity is performed over the irreducible Brillouin zone [56,57] for ThO_2. In doing so, a uniform cu-

Table 2
"Zero-concentration" phonon scattering cross sections for point defects as computed by Deskins et al. for perfect crystals [20]. Finite defect concentrations result in the net effect of vacancies scattering phonons more strongly than interstitials for both cations and anions when computed in practice [60].

Defect type	Phonon scattering cross section
O-vacancy	4.76
O-interstitial	4.76
Th-vacancy	21.50
Th-interstitial	21.50

bic mesh of 1299 representative q-points was used to fill the irreducible Brillouin zone for a face-centered cubic lattice [58]. Summation over the irreducible Brillouin zone exploits point group symmetry properties by assigning weighting factors to each q-point. Relaxation times are calculated by Eq. 3 for each q-point and phonon branch by considering all possible phonon triplets; those which adhere to both energy and crystal momentum conservation are summed via Mattiessen's rule. Dispersion relations from the SCAN functional as shown in Fig. 2 provide frequencies and group velocities for all 1299 sampled q-points, and the above quantities (Eqs. 1 and 2) are found by direct summation.

Scattering by point defects is another mechanism contributing to lattice extrinsic thermal resistivity. Klemens [59] and more recently Gurunathan et al. [60] provide the relaxation time due to scattering from point defects of a particular species j in the form

$$\tau_{PD}^{-1} = \frac{\Omega\pi\,\Gamma_j\omega^2 g(\omega)}{6};\quad g(\omega) = \frac{3\omega^2}{2\pi^2\left[v_p^{qs}(\omega)\right]^2 v_g^{qs}(\omega)}, \tag{4}$$

where Γ_j is the point defect scattering parameter, Ω is the average atomic volume, $g(\omega)$ is the three-dimensional density of states, v_p^{qs} is again the phonon phase velocity, and v_g^{qs} is again the magnitude of phonon group velocity [60,61]. For each point defect species, the scattering parameter may be cast as $\Gamma_j = f_j S_j^2$, where f_j is the defect concentration and S_j^2 is the phonon scattering cross section. The scattering cross sections for each defect depend on the mass differences between the defect and the host lattice, changes in atomic force constants, the macroscopic Grüneisen parameter, and atomic radius mismatch [59,60]. "Zero-concentration" phonon scattering cross sections for the four types of point defects considered are summarized in Table 2. A detailed treatment of the calculation of Γ_j for ThO_2 is provided in the work by Deskins et al. which describes the site averaging scheme used to take into account stoichiometry changes induced by point defects at finite concentrations and results in vacancies having a slightly stronger effect than interstitials [20].

Klemens also provided a model for phonon scattering from dislocation loops by treating the structure of the loop as a stacking fault, which has shown surprisingly good agreement with the resulting reduction of thermal conductivity in ceramics [62,63]. The relaxation time associated with such loops with radius, R_L, and number density, N_L, is

$$\tau_{FL}^{-1}(\omega) = \frac{0.7\pi a^2\gamma^2 R_L^2 N_L}{v_p^{qs}}\omega^2, \tag{5}$$

where a is the crystal lattice parameter and γ is the Grüneisen parameter. For calculations of defect-affected thermal conductivity in this work, experimentally-measured or inferred values for point defect and loop characteristics were used to calculate these additional contributions to scattering for each irradiation condition investigated. The total relaxation time for each of these conditions was calculated using Matthiessen's rule as

$$\frac{1}{\tau_{\text{tot}}} = \sum_i \frac{1}{\tau_i}, \tag{6}$$

where τ_i are the relaxation times due to each scattering mechanism considered [62].

As the initial investigation of this set of crystals indicated the presence of a non-negligible concentration of impurities throughout the bulk of these materials [6], their contribution to phonon scattering has been considered as well. To reduce complexity, rather than attempting to directly calculate impurity scattering using as-measured impurity concentrations, a general impurity scattering term was employed of the form $\tau_{imp}^{-1} = A\omega^4$. A value for A was optimized by fitting the measured temperature-dependent thermal conductivity of our pristine sample to Eq. 1 considering only τ_{3ph} and τ_{imp}, resulting in a value $A = 9.053 \times 10^{-43}$ s^3 [64]. Fig. 3 shows the measured temperature-dependent conductivity from this work together with the optimized calculated conductivity considering (1) only 3-phonon scattering and (2) combined 3-phonon and impurity scattering. This simplified approach captures the as-measured pristine ThO_2 diffusivity well above 100 K, but begins to slightly over-predict conductivity at the lowest temperatures measured. In all calculations of defect-affected conductivity, τ_{imp} is included in the calculation of total relaxation time with this constant value of A. The notable reduction in the present "pristine" conductivity compared to that measured in single crystals in an older work by Mann and coworkers is a known result of a reduction in the quality (ie. higher impurity concentration) of available ThO_2 feedstock material [6,18].

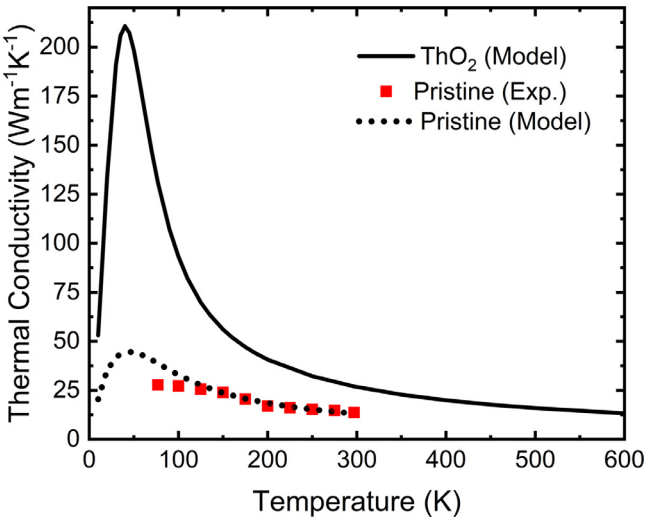

Fig. 3. Model for defect-free ThO_2 thermal conductivity versus temperature including only 3-phonon scattering (solid black line), measured temperature-dependent conductivity of the pristine ThO_2 used here (red squares), and computed conductivity with optimized impurity scattering contribution (dotted black line). (For interpretation of the references to color in this figure legend, the reader is referred to the web version of this article.)

3. Results and discussion

3.1. Experimental measurements

The dislocation loop size and number density were measured from BF TEM images, Fig. 4, using manual image analysis. The average loop size and number density are summarized in Table 3, where the loop size and number density for HT2 and HT3 have been reported in a previous work concerning these samples, but

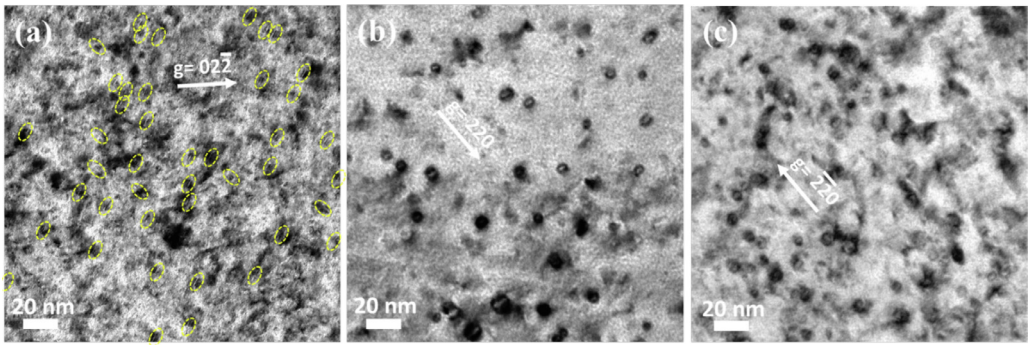

Fig. 4. TEM images of dislocation loops in ThO_2 samples irradiated with proton beam up to (a) 0.16 dpa (60 nm thick lamella), (b) 0.47 dpa (32 nm thick), and (c) 0.79 dpa (43 nm thick). (a) was taken near the [011] zone and (b) and (c) were taken near the [001] zone. The yellow dashed ovals in (a) shows the faulted dislocation loops along the {111} planes. (For interpretation of the references to color in this figure legend, the reader is referred to the web version of this article.)

Table 3
Summary of experimental characterization of proton irradiated ThO_2 including dislocation loop characteristics, optical absorption, and room temperature thermal conductivity. †Optical absorption values represent the 2.0 eV peak. *Values are reported in [6].

Sample ID	Loop Radius [nm]	Loop Density [$\times 10^{22} m^{-3}$]	Optical Absorption† [a.u.]	Conductivity at 297 K [W/m·K]
Pristine	–	–	$\sim 1 \times 10^{-4}$	13.6 ± 0.6
LT1				4.8 ± 0.3*
LT2				3.7 ± 0.2*
LT3				4.1 ± 0.7*
HT1	2.2 ± 0.4	2.6 ± 0.5	1.0×10^{-2}	5.2 ± 0.4
HT2	3.1 ± 0.9*	3.5 ± 0.7*	4.3×10^{-2}	5.1 ± 0.3
HT3	2.6 ± 0.6*	5.2 ± 0.8*	8.0×10^{-2}	7.1 ± 0.7*

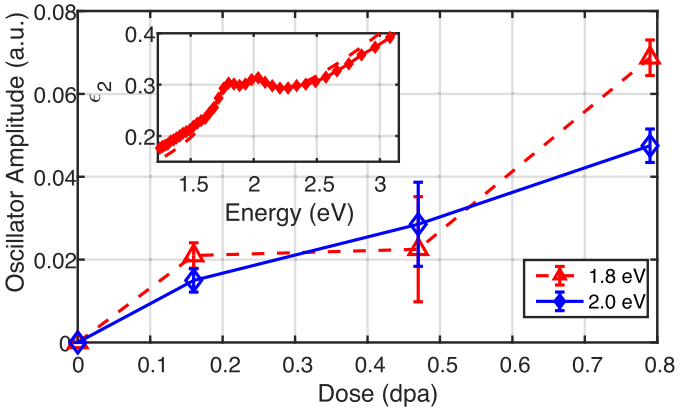

Fig. 5. Amplitude of the Lorentzian oscillators at 1.8 eV (triangle markers) and 2.0 eV (diamond markers) obtained from fitting the spectroscopic ellipsometry data collected on the irradiated ThO_2 crystals.

HT1 is here characterized for the first time [6]. For each specimen, uncertainties in loop size are given by the standard deviation in measured radius and uncertainties in number density are calculated using counting statistics and assuming a 10% error in the EELS-measured lamella thickness. The measured loop radius remains fairly constant between 2–3 nm for all three conditions, while the density is observed to increase monotonically with increasing radiation dose. High-resolution TEM on HT1 shows some loops reside at {111} planes, as was found for HT2 and HT3 previously, and these are likely faulted interstitial Frank loops comprising alternating layers of O–Th–O interstitials [6,63]. A detailed analysis of loop nature, such as Burgers vectors and habit planes, is beyond the scope of this work and is reported separately [65].

The complex dielectric function measured using spectroscopic ellispmetry was modeled using Lorentzian oscillators that represented electronic transitions. Fig. 5 shows the amplitude of the Lorentzian peaks at 1.8 eV and 2.0 eV as a function of displacement damage dose. The inset shows the imaginary part of the dielectric function, ϵ_2, as a function of photon energy measured on HT3. The diamond markers are the experimental data and the dash line is the model fit for two peaks at 1.8 eV and 2 eV. The amplitude of both peaks increases with dose, although the increase in the amplitude of the peak at 1.8 eV is higher from 0.47 dpa to 0.79 dpa. The Lorentzian peak amplitudes are proportional to the number of electronic transitions at that energy. The higher amplitude of the oscillator suggests clear changes in the electronic structure induced by lattice point defects. These dielectric constant measurements share similar features to F- and F^+-centers in sapphire [66,67] and similar features have been reported previously in ThO_2 [68,69].

For SDTR thermal diffusivity measurements, a frequency range 20–100 kHz is selected to ensure that the thermal diffusion length is significantly smaller than the thickness of the plateau damage layer [6,70,71]. All reported values represent spatial averages of five or more locations across the uniformly-irradiated crystal surface. The average Jacobian estimate of the 2σ confidence interval on the optimized thermal diffusivity across most measurements is ~5%. For pristine ThO_2 at temperatures below 100 K this uncertainty increases to ~10% as the high conductivity results in a smaller slope of the measured phase profile while the absolute instrument phase noise remains constant. Measured values of thermal diffusivity as a function of temperature are converted to thermal conductivity using the heat capacity of pristine ThO_2 as a function of temperature [6] and density calculated from temperature-dependent lattice constants [48]. Fig. 6 shows the measured thermal diffusivity and conductivity for pristine, HT1, and HT2 samples. Error bars on measured values represent the standard deviation of spatially-averaged measurements.

Remarkable thermal conductivity reductions are observed on both irradiated ThO_2 samples over the entire temperature range. The thermal conductivity of pristine ThO_2 continuously increases with decreasing temperature as expected. However, it does not exhibit a characteristic $1/T$ dependence, likely due to the presence of significant intrinsic impurity scattering. This curve is calculated to peak at ~50 K, based on LBTE, which is lower than that of

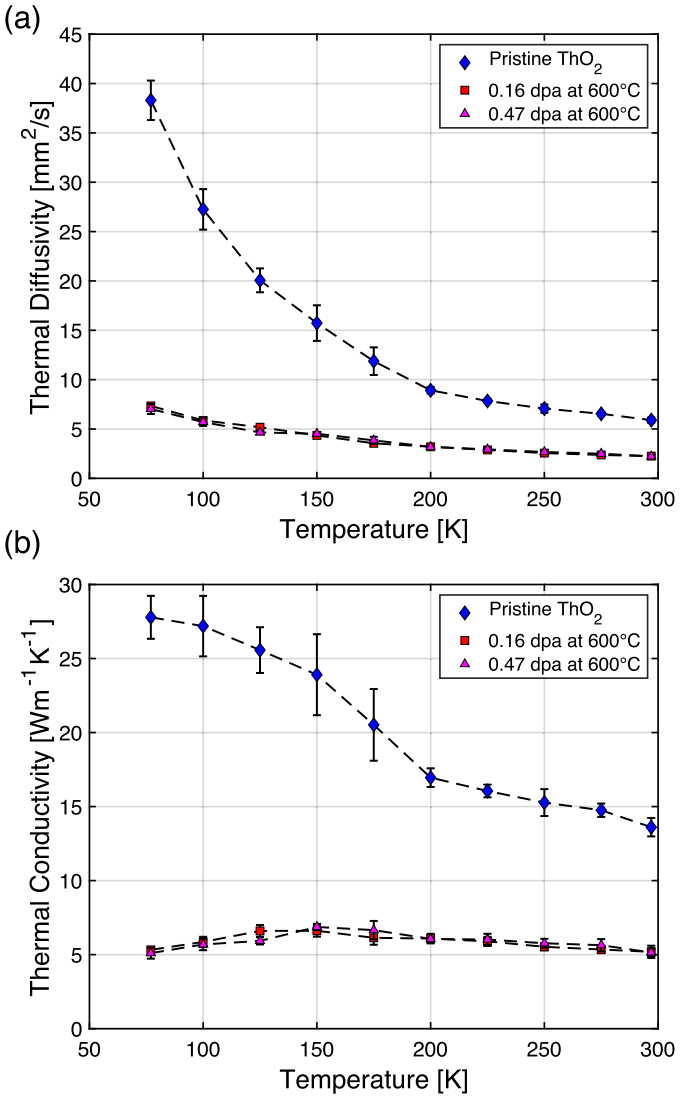

Fig. 6. (a) Thermal diffusivity and (b) conductivity measured on pristine and irradiated ThO_2 using SDTR. Thermal diffusivity (measured directly) is shown to monotonically increased with decreasing temperature in this range. The thermal conductivity shows a softer trend for pristine ThO_2 due to the reduction in heat capacity at low temperatures [6], and the two irradiated samples investigated show little change in conductivity with temperature.

the liquid nitrogen cryogen used in this work and thus was not captured. Thermal conductivity measured at all temperatures is found lower than values reported by Mann and coworkers [18], due to the higher impurity content in these later-generation crystals. Comparing with the pristine sample, the thermal conductivity of the 0.16 dpa and 0.47 dpa samples at room temperature is reduced by ~55% and ~50%, respectively. Both irradiated samples show a much weaker temperature dependence and vary only in a narrow window of ~6–8 W/m·K in the region of 77–297 K, with a slight peak observed around 150 K. It is worth noting that thermal diffusivity of both samples continuously increases in the low temperature region and the values at 77 K are approximately two times higher than the ones at 297 K. This continued increase in thermal diffusivity is offset by a monotonic reduction in heat capacity at low temperatures. Thus, the difference in thermal conductivity (irradiated samples vs pristine sample) increases to an ~80% reduction at 77 K. Notably, although HT2 received approximately three times the irradiation dose of HT1, the measured thermal conductivities with respect to temperature are quite similar, suggesting a saturation in phonon scattering.

3.2. Point defect estimation

A rate theory model is implemented to determine the concentration of point defects, which are expected to have a large contribution to thermal conductivity reduction, using the framework described by Chauhan and coworkers [72,73]. Briefly, this model is captured by a set of ordinary differential equations of the form

$$\frac{\partial C_i}{\partial t} = G - S_{ij} C_i C_j, \tag{7}$$

where C_i are the concentration for each type of defect, in this case monomer oxygen and thorium sublattice vacancies and interstitials (V_O, O_I, V_{Th}, and Th_I) and dislocation loops (L). G is the point defect generation rate defined by the applied displacement damage. Mutual interactions between defects, S_{ij}, represent recombination for each (V_O, O_I) and (V_{Th}, Th_I) pair. Di-interstitial formation for two Th_I defects acts as the sole loop nucleation mechanism. Terms S_{iL} represent the absorption of point defects by loops and contribute to loop growth or shrinkage subject to the conservation of atoms

$$\frac{d}{dt}\left(\frac{\pi b}{3\Omega} R_L^2 C_L\right) = S_{iL} C_i C_L, \tag{8}$$

where R_L is the loop radius, b is the Burgers vector, and Ω is the average atomic volume. Each non-zero S_{ij} depends on point defect mobility and geometrical factors capturing the atomic structure of each defect. In particular, this model is implemented by taking S_{iL} proportional to R_L to reflect an increasing point defect capture probability with loop size.

Primary defect generation rates are calculated from SRIM simulations and the applied ion beam current as 1.13×10^{-6} dpa/sec for O and 0.52×10^{-6} dpa/sec for the identified 18 μm plateau region, resulting in an O/Th Frenkel pair production ratio of 2.17. The model is parametrized by optimizing a set of four parameters: the migration energies of Th_I, O_I, and V_O as well as a conversation factor relating optical absorption at 2.0 eV to oxygen vacancy concentration. This optimization considers three sets of experimental observables, the TEM-measured loop density for 600 °C irradiations, the TEM-measured loop radius for 600 °C irradiations, and optical absorption amplitude at 2.0 eV. In the considered irradiation parameter space, V_{Th} are assumed to have a large migration energy consistent with previously reported calculated values of ~5 eV [74] essentially deeming them immobile. Optimized values for migration energies are presented in Table 4 where they are compared to previous literature [74–76]. This set of experimental observables contains information pertaining to each defect population. Frank loop density and size are directly governed by the slowest migrating species, in this case thorium interstitials, which in turn controls the resulting oxygen interstitial population given the stoichiometric nature of the observed loops. Optical absorption measurements provide direct access to retained oxygen vacancy populations. Fig. 7 shows the rate theory calculated point defect and dislocation loop atomic concentrations as a function of dose for both exposure temperatures considered. At high doses, stoichiometric interstitial dislocation loop formation leads to a relatively large imbalance in the oxygen point defect populations. Lower mutual recombination rates at 20 °C lead to a higher equilibrium concentration of point defects of all types, while the lower mobility precludes loop formation.

Fig. 8 shows the three sets of experimental observables in comparison with the predicted values using optimal fitting parameters. For TEM-measured loop characteristics, there is a reasonable agreement for dislocation loop size (given experimental uncertainty).

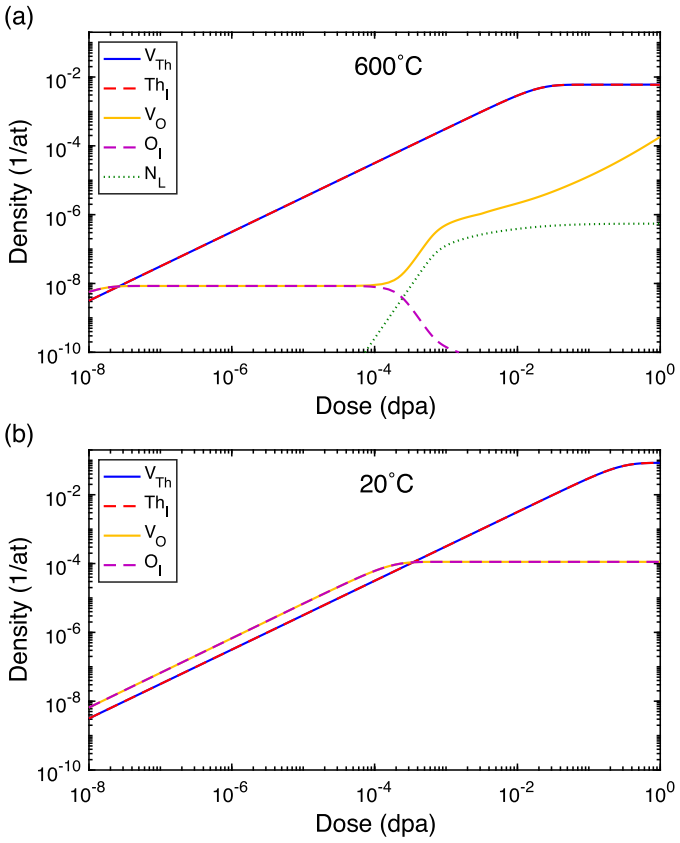

Fig. 7. Output of rate theory calculations of point defect and dislocation loop density at (a) 600 °C and (b) 20 °C. At 600 °C, the greater mobility of defects leads to interstitial loop formation at higher doses and an imbalance in the retained point vacancy and interstitial concentrations.

Table 4
Defect parameters used in conjunction with microstructure evolution modeling. Values labeled by * are output from the minimization of the rate theory model to experimental data.

	Th_I	O_I	V_O	V_{Th}
D_0 [cm^2/s]	0.01 [78]	0.01 [79]	0.02 [79]	0.65 [80]
E_m [eV] (DFT)	–	1 [76]	2.1 [74]	5.1 [75]
E_m [eV] (used)	2.86*	0.72*	1.49*	5.1

However, while the experimentally-measured loop density gradually increases, the current model suggests saturation, behavior similar to that observed in other materials [72,73]. This can be attributed to limitations of the rate model of Chauhan and coworkers which includes only a single mechanism invoked for loop nucleation and evolution. The majority of the loops observed in this work are {111}-plane faulted loops whose growth beyond a certain size becomes unfavorable. At larger sizes, loop growth in similar systems has been shown to be accompanied by unfaulting and formation of {011}-plane perfect loops [77]. Including additional mechanisms such as unfaulting or direct in-cascade loop nucleation would introduce too many free parameters in this simplified model based on the experimental observables available for parameter minimization. The first-order estimates of point defect populations made possible by using this framework are necessary given the large role that these smallest-scale features play in limiting thermal conductivity [20].

The final set of experimental observables used for rate theory minimization are the optical absorption data directly correlated to oxygen vacancy concentration in Fig. 8(c). This comparison is made possible by assuming that experimental spectra reveal oxygen vacancies acting as *F*-centers [81,82]. Literature on optical spectra characterization of irradiated thoria is limited [68,69], therefore we postulate that observed peaks can be assigned to either an *F*- or F^+-center. Fig. 8(c) compares the amplitude of an *F*-center signal defined by the experimentally-measured intensity of the 2.0 eV optical absorption peak to the final oxygen vacancy concentration predicted by rate theory. To make this comparison, the measured intensities of absorption peaks are multiplied by a normalizing factor (with units concentration per amplitude) since these intensities only provide relative information in experiment. This conversion factor is the final model parameter minimized to this set of data in addition to the noted defect migration energies. Of note is that this simplified comparison does not attempt to distinguish between *F*- and F^+-centers. Unlike loop density, optical absorption data is found to track the rate-theory-modeled oxygen vacancy concentration quite well, suggesting that major mechanisms controlling the retained oxygen defects are accounted for in this simplified model.

3.3. Comparison of computed and measured thermal transport

Fig. 9 shows LBTE modeling results for temperature-dependent thermal conductivity of ThO_2 compared with experimentally-measured values for both a pristine sample and samples HT1

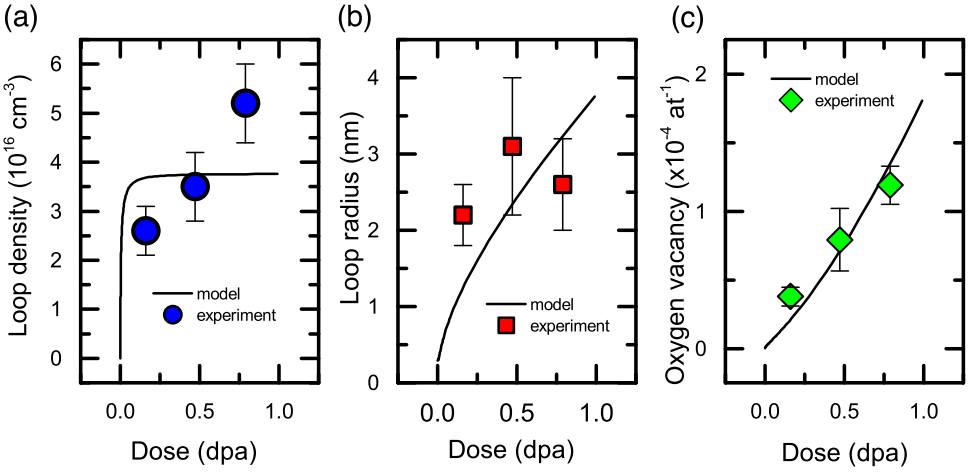

Fig. 8. Experimental observables from ThO_2 irradiated at 600 °C used to minimize the rate theory model of point defect and loop evolution. Measured (a) loop densities, (b) loop radii, and (c) oxygen vacancy concentration proportional to optical absorption values are all used to fit the final migration energies listed in Table 4.

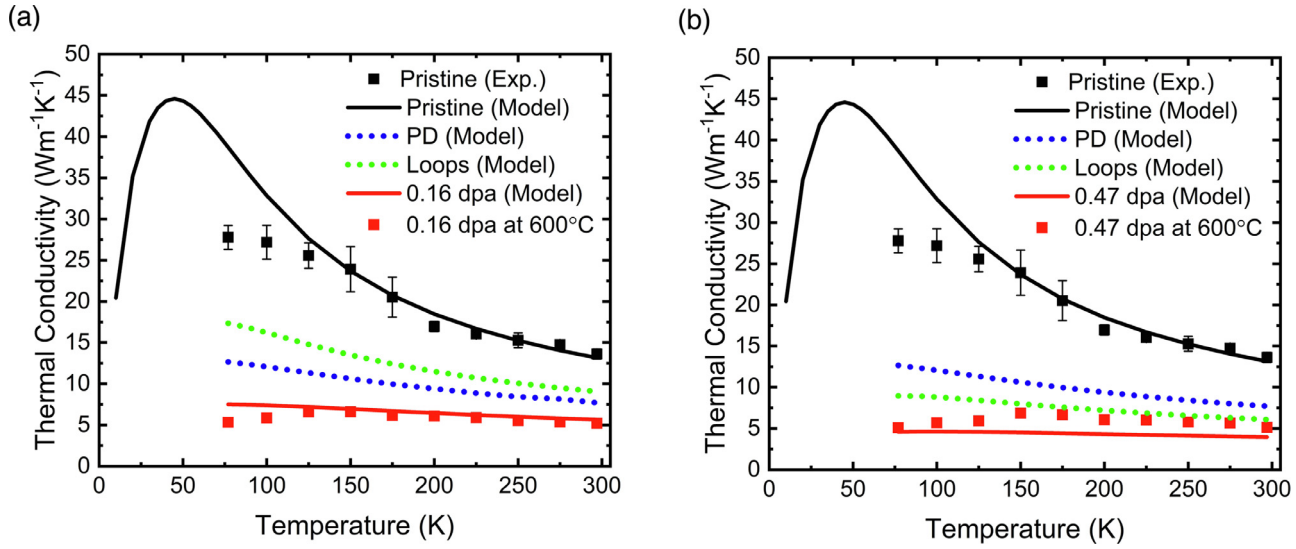

Fig. 9. Conductivity versus temperature considering only rate-theory-modeled point defects (PD), only experimentally-measured faulted dislocation loops, and combined defect contributions compared to experimentally-measured conductivities for (a) HT1 – 0.16 dpa and (b) HT2 – 0.47 dpa. Pristine experimental and simulated conductivities are shown for comparison.

and HT2, irradiated to 0.16 and 0.47 dpa at 600 °C, respectively. The blue and green dotted curves show the modeled conductivity when only point defects (predicted by rate theory) and only dislocation loops (experimentally-measured) are added to the pristine model. For both 0.16 and 0.47 dpa, the point defect (PD) only model is comparable, while the dislocation loop only model makes a much more significant contribution at 0.47 dpa when compared to 0.16 dpa. Both phenomena can be interpreted by looking at the associated point defect densities, Fig. 7(a), and the average loop radii and densities listed in Table 3. At the two doses considered in Fig. 9, the concentrations of Th defects have saturated. Though the concentrations of O defects are still evolving, their concentrations are too low to contribute to a noticeable change in conductivity given their lower phonon scattering cross sections, see Table 2 [20]. By Eq. 5, phonon scattering rates associated with dislocation loops are inversely proportional to the loop density and the loop radius squared, both of which have increased at 0.47 dpa compared to 0.16 dpa. These increases in both loop radius and density at 0.47 dpa cause the notable difference in loop model predictions shown in Fig. 9. The modeling result for the 0.16 dpa sample, which considers both point defect and loop scattering, is in good agreement with experimentally-measured values. The agreement for the 0.47 dpa sample is reasonable, although the LBTE model under-predicts the measured conductivity at most temperatures. However, the general agreement of the model and experiment in both cases is remarkable considering that we have only used a single fitting parameter to calibrate our defect-free model to the pristine sample.

Finer detail into the contribution of each species of point defect considered is shown in Fig. 10. Conductivity as a function of temperature is again shown, here considering the scattering contributions of each point defect (V_O, O_I, V_{Th}, and Th_I) individually, as well as re-producing the curves for all point defects and the total reduction inclusive of point defects and loops from Fig. 9. This breakdown highlights the minimal effect on phonon scattering induced by oxygen sublattice defects; they are present in these conditions at such low concentrations that their contribution to phonon scattering is negligible. This paired with their lower phonon scattering cross-section when compared to thorium defects make Th vacancies and interstitials the dominant point defect scattering mechanisms. At the dose rates and temperatures applied in experiment, Th vacancies and interstitials have approximately the same concentration. However, vacancies result in slightly stronger phonon scattering, reflected for both conditions in Fig. 10, as a result of the lattice site averaging detailed by Gurunathan et al. [60].

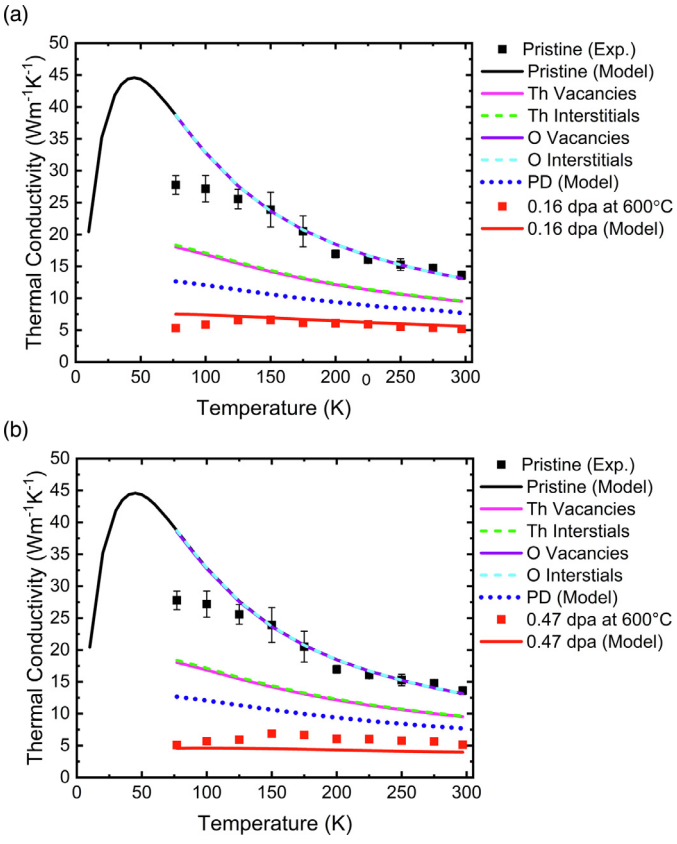

Fig. 10. Comparison of conductivity reduction due to each individual type of point defect considered in this analysis for (a) HT1 and (b) HT2. The combined point defect (PD) curves match those shown in Fig. 9.

In addition to the two cases where temperature-dependent conductivity was measured in this study, enough rate theory and experimental data are available to calculate values for conductivity

Table 5
Comparison of LBTE-calculated and experimentally measured thermal conductivities for each sample at 297 K, all values in W/m·K. Individual contributions to the reduction in conductivity due to point defects (PD) and dislocation loops (DL) are listed separately as well as the final computed conductivity considering both point and extended defects.

	LT1	LT2	LT3	HT1	HT2	HT3
Simulated *k* PD only	8.19	3.66	2.29	7.70	7.70	7.69
Simulated *k* DL only	–	–	–	9.06	6.08	5.61
Simulated *k* total	8.19	3.66	2.29	5.72	4.00	3.72
Experimental *k*	4.8±0.3	3.7±0.2	4.1±0.7	5.2±0.4	5.1±0.3	7.1±0.7

for all six irradiation conditions listed in Table 1. A comparison between the measured 297 K thermal conductivities for defected ThO_2 calculated using LBTE and those measured in experiment is shown in Table 5, including contributions from point defects and dislocation loops separately as well as the total computed conductivity. Although computed conductivity values for HT-series samples are relatively close for the two lower doses considered (HT1 and HT2), the experimentally-measured conductivity for HT3 is significantly larger than both the computed values and those for the two lower doses. However, as noted in Table 3, this value comes from an earlier work where the conductivity was measured using a simplified analysis method [6]. In that initial study, sample HT2 was also measured and found to have a conductivity of 7.4 W/m·K, larger than that found in later measurements using a full 3D analysis of thermal wave profiles. Thus, the greatest portion of this difference for HT3 likely comes from the measurement technique itself. For RT-series samples, while experimental conductivity values seem to be saturated, LBTE results based on rate theory defect modeling indicate a continued evolution in conductivity with dose.

In Fig. 11, LBTE modeling results at constant temperatures of 125 K, 225 K, and 297 K are compared to experimentally-measured thermal conductivity as a function of proton radiation dose in dpa for exposures at both temperatures. Continuous curves for each temperature use both dislocation loop and point defect concentrations provided by our rate theory model, while the stars in Fig. 11(a) implement dislocation loop distributions determined from TEM measurements while retaining rate-theory point defect concentrations. The squares in each figure are SDTR-measured values for conductivity. In both Fig. 11(a) and (b), experimental measurements of conductivity seemed to have reached a saturated value and are relatively constant with increasing dose. LBTE modeling based on rate theory estimations miss this conductivity saturation for several reasons in each temperature regime. At high temperatures, Fig. 11(a), the continued decrease in conductivity with increasing radiation dose is driven by a continued increase in dislocation loop size, Fig. 8(b), coupled with the R_L^{-2} dependence on the scattering time due to loops given in Eq. 5. As mentioned above, the current model does not consider any loop unfaulting processes that are expected to impact loop growth in higher dose cases. While a more detailed dislocation loop kinetic analysis including multiple nucleation mechanisms, unfaulting, and size saturation is beyond the scope of this work, such an analysis is expected to have little effect on the reported point defect evolution as the mutual recombination rate is the dominant factor in resultant point defect density.

For room temperature exposures shown in Fig. 11(b), a saturation in conductivity is evident, albeit at larger doses than experimental data would indicate. This behavior stems directly from Fig. 7(b), where concentrations of thorium point defects are still evolving at these doses and have not yet reached saturation. One possible contribution to this behavior is the optimization of the present rate theory model to 600 °C irradiation data only and the fixing of the V_{Th} migration energy to that computed previously

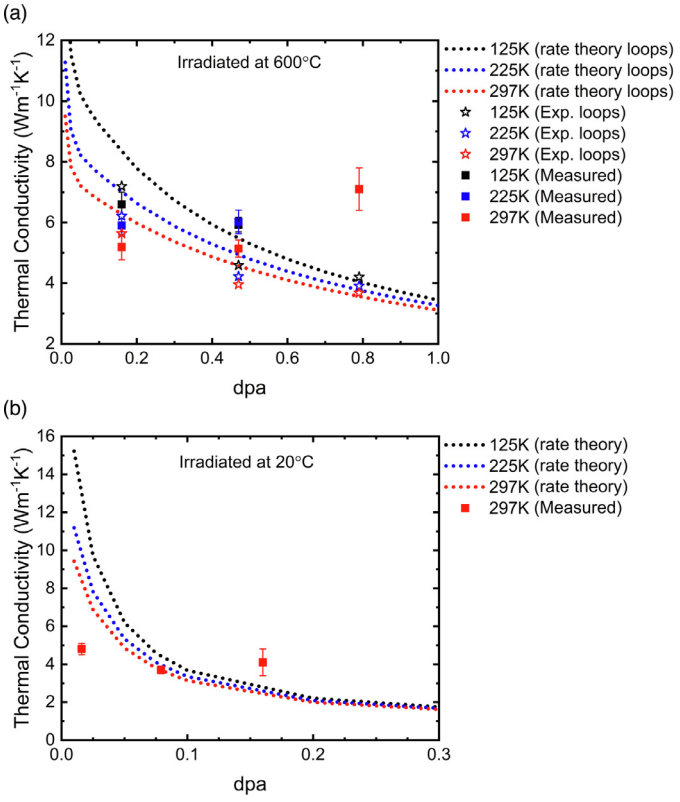

Fig. 11. Conductivity of ThO_2 as a function of proton radiation dose in dpa for exposures at (a) 600 °C and (b) 20 °C. Continuous curves show the predicted conductivity using both point defect and loop density from rate theory modeling, stars (600 °C only) show calculated conductivity for TEM-measured loop distributions and rate theory point defects, and squares show measured conductivity.

using DFT. Should that migration energy in practice be lower, defect saturation at room temperature would be expected to occur at both lower doses and saturate to lower thorium defect concentrations. Such increased thorium defect mobility would have little effect on the relatively good agreement we find between rate theory estimations of oxygen defects and optical measurements as shown in Fig. 8(c).

Another mechanism which likely accounts for some of the observed differences in computed and measured thermal conductivities is the lack of any small-scale clustering processes present in the analysis conducted here. At these dose levels, for both temperatures, some clustering of point defects into larger, non-loop defect clusters is likely present. Our previous work on a sub-set of these samples included Raman spectroscopy analysis which indicated the presence of M_4O_9-type cuboctahedral clusters in these defected samples [6]. Recent molecular dynamics simulations by Jin and coworkers have also shown this type of interstitial cluster as a stable geometry in ThO_2 [83]. Were clustering mechanisms included in the defect evolution model employed here, computed

thermal conductivities would likely increase as the finite number of point defects agglomerate into fewer total phonon scattering sites (albeit with modified strength). These mechanisms, in addition to the others detailed, would likely flatten the dose-dependent conductivity at both temperatures at larger dose levels and lead to better agreement with measured values. Future work in this area will focus on the implementation of cluster dynamics modeling [84] of defect evolution in ThO_2 such that a wider spectrum of defect morphologies may be used as inputs into the deployed LBTE framework. Finally, the possibility of resonant scattering phenomena by charged *F*-center defects should be taken into consideration in the future as well [85], as resonant scattering may more significantly impact thermal transport than the uncharged oxygen vacancy model implemented here.

4. Conclusions

Here, a combined experimental, computational, and analytical approach has been used to investigate phonon-mediated thermal transport in thorium dioxide as a model nuclear ceramic. Updated DFT calculations of the phonon band structure of ThO_2 are used to seed the calculation of temperature-dependent thermal conductivity utilizing a linearized Boltzmann transport equation framework. Multiple contributions to the relaxation time are taken into account including intrinsic 3-phonon and impurity scattering as well as extrinsic point defect and dislocation loop scattering induced as a result of proton irradiation. Experimental measurements of a defected region of ThO_2 induced by proton irradiation show a dramatic decrease in thermal conductivity, which is captured using LBTE modeling through a combined approach of point defect estimation using a rate theory defect model and direct TEM measurements of dislocation loop size and density. While only considering point defects and dislocation loops of a single type, LBTE and experimental conductivity measurements show reasonable agreement considering the single fitting parameter used to account for native impurity species. Features of defect and conductivity saturation are observed in different conditions through modeling and experiment, indicating that additional types of defects beyond point defects and dislocation loops should be considered to capture the complexity of defect-induced phonon scattering. Reasonable pathways exist for increasing the confidence in the experimental estimation of small-scale defects (through the inclusion of Raman spectroscopy) and the computational estimation of all possible defect cluster configurations (through cluster dynamics). Each of these future pathways may be incorporated into the combined framework described in this work, leading to the ultimate goal of complete, multi-scale understanding and control of thermal transport in defect-bearing actinide oxides.

Declaration of Competing Interest

The authors declare that they have no known competing financial interests or personal relationships that could have appeared to influence the work reported in this paper.

Acknowledgments

This work was supported by the Center for Thermal Energy Transport under Irradiation (TETI), an Energy Frontier Research Center funded by the US Department of Energy, Office of Science, Office of Basic Energy Sciences. The authors would like to thank Lin Shao and Aaron French at Texas A&M University for providing ion irradiation support as part of a Nuclear Science User Facilities (NSUF) experiment funded through the US Department of Energy, Office of Nuclear Energy under DOE Idaho Operations Office Contract DE-AC07-05ID14517. This research used resources of the National Energy Research Scientific Computing Center, a DOE Office of Science User Facility supported by the Office of Science of the U.S. Department of Energy under Contract No. DE-AC02-05CH11231.

References

[1] K. Gofryk, S. Du, C.R. Stanek, J.C. Lashley, X.Y. Liu, R.K. Schulze, J.L. Smith, D.J. Safarik, D.D. Byler, K.J. McClellan, B.P. Uberuaga, B.L. Scott, D.A. Andersson, Anisotropic thermal conductivity in uranium dioxide, Nat. Commum. 5 (2014) 4551, doi:10.1038/ncomms5551.
[2] P.R. Hania, F.C. Klaassen, 3.04 - Thorium Oxide Fuel, in: R.J. Konings (Ed.), Comprehensive Nuclear Materials, Elsevier, Oxford, 2012, pp. 87–108.
[3] J.S. Herring, P.E. MacDonald, K.D. Weaver, C. Kullberg, Low cost, proliferation resistant, uranium thorium dioxide fuels for light water reactors, Nucl. Eng. Des. 203 (1) (2001) 65–85, doi:10.1016/S0029-5493(00)00297-1.
[4] S.F. Ashley, G.T. Parks, W. Nuttall, C. Boxall, R.W. Grimes, Thorium fuel has risks, Nature 492 (2012) 31–33, doi:10.1038/492031a.
[5] C. Ronchi, M. Sheindlin, D. Staicu, M. Kinoshita, Effect of burn-up on the thermal conductivity of uranium dioxide up to 100000 $MWdt^{-1}$, J. Nucl. Mater. 327 (1) (2004) 58–76, doi:10.1016/j.jnucmat.2004.01.018.
[6] C.A. Dennett, Z. Hua, A. Khanolkar, T. Yao, P.K. Morgan, T.A. Prusnick, N. Poudel, A. French, K. Gofryk, L. He, L. Shao, M. Khafizov, D.B. Turner, J.M. Mann, D.H. Hurley, The influence of lattice defects, recombination, and clustering on thermal transport in single crystal thorium dioxide, APL Mater. 8 (2020) 111103, doi:10.1063/5.0025384.
[7] K. Shrestha, T. Yao, J. Lian, D. Antonio, M. Sessim, M.R. Tonks, K. Gofryk, The grain-size effect on thermal conductivity of uranium dioxide, J. Appl. Phys. 126 (12) (2019) 125116, doi:10.1063/1.5116372.
[8] X.-Y. Liu, M.W.D. Cooper, K.J. McClellan, J.C. Lashley, D.D. Byler, B.D.C. Bell, R.W. Grimes, C.R. Stanek, D.A. Andersson, Molecular dynamics simulation of thermal transport in UO_2 containing uranium, oxygen, and fission-product defects, Phys. Rev. Applied 6 (2016) 044015, doi:10.1103/PhysRevApplied.6.044015.
[9] R.L. Williamson, J.D. Hales, S.R. Novascone, M.R. Tonks, D.R. Gaston, C.J. Permann, D. Andrs, R.C. Martineau, Multidimensional multiphysics simulation of nuclear fuel behavior, J. Nucl. Mater. 423 (1) (2012) 149–163, doi:10.1016/j.jnucmat.2012.01.012.
[10] M.R. Tonks, X.-Y. Liu, D. Andersson, D. Perez, A. Chernatynskiy, G. Pastore, C.R. Stanek, R. Williamson, Development of a multiscale thermal conductivity model for fission gas in UO_2, J. Nucl. Mater. 469 (2016) 89–98, doi:10.1016/j.jnucmat.2015.11.042.
[11] D.A. Broido, M. Malorny, G. Birner, N. Mingo, D.A. Stewart, Intrinsic lattice thermal conductivity of semiconductors from first principles, Appl. Phys. Lett. 91 (23) (2007) 231922, doi:10.1063/1.2822891.
[12] L. Lindsay, D.A. Broido, T.L. Reinecke, *Ab initio* thermal transport in compound semiconductors, Phys. Rev. B 87 (2013) 165201, doi:10.1103/PhysRevB.87.165201.
[13] S. Huberman, V. Chiloyan, R.A. Duncan, L. Zeng, R. Jia, A.A. Maznev, E.A. Fitzgerald, K.A. Nelson, G. Chen, Unifying first-principles theoretical predictions and experimental measurements of size effects in thermal transport in SiGe alloys, Phys. Rev. Materials 1 (2017) 054601, doi:10.1103/PhysRevMaterials.1.054601.
[14] H. Nakamura, M. Machida, First-principles calculation study on phonon thermal conductivity of thorium and plutonium dioxides: intrinsic anharmonic phonon-phonon and extrinsic grain-boundary-phonon scattering effects, J. Nucl. Mater. 519 (2019) 45, doi:10.1016/j.jnucmat.2019.03.033.
[15] B. Szpunar, J.A. Szpunar, K.-S. Sim, Theoretical investigation of structural and thermo-mechanical properties of thoria, J. Phys. Chem. Solids 90 (2016) 114–120, doi:10.1016/j.jpcs.2015.10.011.
[16] J. Park, E.B. Farfán, K. Mitchell, A. Resnick, C. Enriquez, T. Yee, Sensitivity of thermal transport in thorium dioxide to defects, J. Nucl. Mater. 504 (2018) 198–205, doi:10.1016/j.jnucmat.2018.03.043.
[17] K. Bakker, E.H.P. Cordfunke, R.J.M. Konings, R.P.C. Schram, Critical evaluation of the thermal properties of ThO_2 and $th_{1-y}U_yO_2$ and a survey of the literature data on $Th_{1-y}Pu_yO_2$, J. Nucl. Mater. 250 (1) (1997) 1–12, doi:10.1016/S0022-3115(97)00241-9.
[18] J.M. Mann, D. Thompson, K. Serivalsatit, T.M. Tritt, J. Ballato, J. Kolis, Hydrothermal growth and thermal property characterization of ThO_2 single crystals, Cryst. Growth Des. 10 (5) (2010) 2146–2151, doi:10.1021/cg901308f.
[19] M. Khafizov, V. Chauhan, Y. Wang, F. Riyad, N. Hang, D. Hurley, Investigation of thermal transport in composites and ion beam irradiated materials for nuclear energy applications, J. Mater. Res. 32 (1) (2017) 204–216, doi:10.1557/jmr.2016.421.
[20] W.R. Deskins, A. Hamed, T. Kumagai, C.A. Dennett, M. Khafizov, D.H. Hurley, A. El-Azab, Thermal conductivity of ThO_2: effect of point defect disorder, J. Appl. Phys. 129 (7) (2021) 075102, doi:10.1063/5.0038117.
[21] M. Khafizov, M.F. Riyad, Y. Wang, J. Pakarinen, L. He, T. Yao, A. El-Azab, D. Hurley, Combining mesoscale thermal transport and x-ray diffraction measurements to characterize early-stage evolution of irradiation-induced defects in ceramics, Acta Mater. 193 (2020) 61–70, doi:10.1016/j.actamat.2020.04.018.

[22] H.Y. Xiao, Y. Zhang, W.J. Weber, Ab initio molecular dynamics simulations of low-energy recoil events in ThO_2, CeO_2, and ZrO_2, Phys. Rev. B 86 (2012) 054109, doi:10.1103/PhysRevB.86.054109.

[23] W.J. Weber, Y. Zhang, Predicting damage production in monoatomic and multielemental targets using stopping and range of ions in matter code: challenges and recommendations, Curr. Opin. Solid State Mater. Sci. 23 (4) (2019) 100757, doi:10.1016/j.cossms.2019.06.001.

[24] J.F. Ziegler, M.D. Ziegler, J.P. Biersack, SRIM: The stopping and range of ions in matter (2010), Nucl. Instrum. Meth. Phys. Res. B 268 (11–12) (2010) 1818–1823, doi:10.1016/j.nimb.2010.02.091.

[25] D.H. Hurley, R.S. Schley, M. Khafizov, B.L. Wendt, Local measurement of thermal conductivity and diffusivity, Rev. Sci. Instrum. 86 (12) (2015) 123901, doi:10.1063/1.4936213.

[26] Z. Hua, H. Ban, M. Khafizov, R. Schley, R. Kennedy, D.H. Hurley, Spatially localized measurement of thermal conductivity using a hybrid photothermal technique, J. Appl. Phys. 111 (10) (2012) 103505, doi:10.1063/1.4716474.

[27] M. Reichling, H. Grönbeck, Harmonic heat flow in isotropic layered systems and its use for thin film thermal conductivity measurements, J. Appl. Phys. 75 (4) (1994) 1914–1922, doi:10.1063/1.356338.

[28] S.J. Mason, D.J. Wesenberg, A. Hojem, M. Manno, C. Leighton, B.L. Zink, Violation of the Wiedemann-Franz law through reduction of thermal conductivity in gold thin films, Phys. Rev. Mater. 4 (2020) 065003, doi:10.1103/PhysRevMaterials.4.065003.

[29] A.A. Maznev, J. Hartmann, M. Reichling, Thermal wave propagation in thin films on substrates, J. Appl. Phys. 78 (9) (1995) 5266–5269, doi:10.1063/1.359702.

[30] P.A. Popov, P.P. Fedorov, V.V. Osiko, Thermal conductivity of single crystals of the $Ca_{1-x}Y_xF_{2+x}$ solid solution, Dokl. Phys. 55 (2014) 199–202, doi:10.1134/S1028335814050036.

[31] K. Iakoubovskii, K. Mitsuishi, Y. Nakayama, K. Furuya, Thickness measurements with electron energy loss spectroscopy, Microsc. Res. Tech. 71 (8) (2008) 626–631, doi:10.1002/jemt.20597.

[32] J.P. Perdew, A. Zunger, Self-interaction correction to density-functional approximations for many-electron systems, Phys. Rev. B 23 (1981) 5048, doi:10.1103/PhysRevB.23.5048.

[33] J.P. Perdew, J.A. Chevary, S.H. Vosko, M.R. Jackson K. A. andPederson, D.J. Singh, C. Fiolhais, Atoms, molecules, solids, and surfaces: applications of the generalized gradient approximation for exchange and correlation, Phys. Rev. B 46 (1992) 6671, doi:10.1103/PhysRevB.46.6671.

[34] J.W. Sun, A. Ruzsinszky, J.P. Perdew, Strongly constrained and appropriately normed semilocal density functional, Phys. Rev. Lett. 115 (2015) 036402, doi:10.1103/PhysRevLett.115.036402.

[35] P.E. Blochl, Projector augmented-wave method, Phys. Rev. B 50 (1994) 17953, doi:10.1103/PhysRevB.50.17953.

[36] G. Kresse, D. Joubert, From ultrasoft pseudopotentials to the projector augmented-wave method, Phys. Rev. B 59 (1999) 1758, doi:10.1103/PhysRevB.59.1758.

[37] G. Kresse, J. Hafner, *Ab initio* molecular-dynamics for liquid-metals, Phys. Rev. B 47 (1993) 558, doi:10.1103/PhysRevB.47.558.

[38] G. Kresse, J. Hafner, *Ab-initio* molecular-dynamics simulation of the liquid-metal amorphous-semiconductor transition in germanium, Phys. Rev. B 49 (1994) 14251, doi:10.1103/PhysRevB.49.14251.

[39] G. Kresse, J. Furthmuller, Efficiency of *ab-initio* total energy calculations for metals and semiconductors using a plane-wave basis set, Comput. Mater. Sci. 6 (1996) 15, doi:10.1016/0927-0256(96)00008-0.

[40] G. Kresse, J. Furthmuller, Efficient iterative schemes for *Ab initio*total-energy calculations using a plane-wave basis set, Phys. Rev. B 54 (1996) 11169, doi:10.1103/PhysRevB.54.11169.

[41] R.I. Palomares, C.L. Tracy, F. Zhang, C. Park, D. Popov, C. Trautmann, R.C. Ewing, M. Lang, *In situ* defect annealing of swift heavy ion irradiated CeO_2 and ThO_2 using synchrotron x-ray diffraction and a hydrothermal diamond anvil cell, J. Appl. Crystallogr. 48 (3) (2015) 711–717, doi:10.1107/S160057671500477X.

[42] L. Fu, M. Kornbluth, Z. Cheng, C.A. Marianetti, Group theoretical approach to computing phonons and their interactions, Phys. Rev. B 100 (2019) 014303, doi:10.1103/PhysRevB.100.014303.

[43] X. Gonze, C. Lee, Dynamical matrices, born effective charges, dielectric permittivity tensors, and interatomic force constants from density-functional perturbation theory, Phys. Rev. B 55 (1997) 10355, doi:10.1103/PhysRevB.55.10355.

[44] K. Clausen, W. Hayes, J.E. Macdonald, R. Osborn, P.G. Schnabel, M.T. Hutchings, A. Magerl, Inelastic neutron-scattering investigation of the lattice-dynamics of ThO_2 and CeO_2, J. Chem. Soc. Faraday Trans. 83 (1987) 1109, doi:10.1039/F29878301109.

[45] M. Bryan, L. Fu, K. Rickert, D. Turner, T. Prusnick, J. Mann, D. Abernathy, C.A. Marianetti, M. Manley, Nonlinear propagating modes beyond the phonons in fluorite-structured crystals, Commun. Phys. 3 (2020) 217, doi:10.1038/s42005-020-00483-2.

[46] C. Sevik, T. Cagin, Mechanical and electronic properties of CeO_2, ThO_2, and $(Ce,Th)O_2$ alloys, Phys. Rev. B 80 (2009) 014108, doi:10.1103/PhysRevB.80.014108.

[47] Y. Lu, Y. Yang, P. Zhang, Thermodynamic properties and structural stability of thorium dioxide, J. Phys. Condens. Matter 24 (22) (2012) 225801, doi:10.1088/0953-8984/24/22/225801.

[48] B. Szpunar, J.A. Szpunar, Theoretical investigation of structural and thermo-mechanical properties of thoria up to 3300K temperature, Solid State Sci. 36 (2014) 35, doi:10.1016/j.solidstatesciences.2014.07.004.

[49] Q. Li, J.S. Yang, D.H. Huang, Q.L. Cao, F.H. Wang, Phase transition and thermodynamic properties of ThO_2: quasi-harmonic approximation calculations and anharmonic effects, Chin. Phys. B 23 (2014) 017101, doi:10.1088/1674-1056/23/1/017101.

[50] P.S. Ghosh, A. Arya, G.K. Dey, N. Kuganathan, R.W. Grimes, A computational study on the superionic behaviour of ThO_2, Phys. Chem. Chem. Phys. 18 (2016) 31494, doi:10.1039/C6CP05794B.

[51] L. Malakkal, B. Szpunar, J.C. Zuniga, R.K. Siripurapu, J.A. Szpunar, First principles calculation of thermo-mechanical properties of thoria using quantum espresso, Int. J. Compu. Mat. Sci. Eng. 5 (2016) 1650008, doi:10.1142/S2047684116500081.

[52] J.Y. Liu, Z.H. Dai, X.X. Yang, Y.C. Zhao, S. Meng, Lattice thermodynamic behavior in nuclear fuel ThO_2 from first principles, J. Nucl. Mater. 511 (2018) 11, doi:10.1016/j.jnucmat.2018.08.054.

[53] L. Malakkal, A. Prasad, E. Jossou, J. Ranasinghe, B. Szpunar, L. Bichler, J. Szpunar, Thermal conductivity of bulk and porous ThO_2: atomistic and experimental study, J. Alloy Compd. 798 (2019) 507, doi:10.1016/j.jallcom.2019.05.274.

[54] G.P. Srivastava, The Physics of Phonons, Taylor and Francis, 1990.

[55] G.A. Slack, The Thermal Conductivity of Nonmetallic Crystals, in: Solid State Physics, 34, Academic Press, 1979, pp. 1–71, doi:10.1016/S0081-1947(08)60359-8.

[56] A. Hamed, Computational modeling of thermal transport using spectral phonon Boltzmann transport equation, Purdue University, 2017 Ph.D. thesis.

[57] A. Hamed, A. El-Azab, Peak intrinsic thermal condictivity in non-metallic solids and a new interpretation of experimental data for argon, J. Phys. Commun. 2 (2018) 015022, doi:10.1088/2399-6528/aaa36f.

[58] D.C. Wallace, Thermodynamics of crystals, Dover Publications Inc., 1998.

[59] P.G. Klemens, The scattering of low-frequency lattice waves by static imperfections, Proc. Phys. Soc. A 68 (12) (1955) 1113–1128, doi:10.1088/0370-1298/68/12/303.

[60] R. Gurunathan, R. Hanus, M. Dylla, A. Katre, G.J. Snyder, Analytical models of phonon–point-defect scattering, Phys. Rev. Appl. 13 (2020) 034011, doi:10.1103/PhysRevApplied.13.034011.

[61] S.-i. Tamura, Isotope scattering of large-wave-vector phonons in GaAs and InSb: deformation-dipole and overlap-shell models, Phys. Rev. B 30 (1984) 849–854, doi:10.1103/PhysRevB.30.849.

[62] P.G. Klemens, Thermal Conductivity and Lattice Vibrational Modes, in: Solid State Physics, 7, Academic Press, 1958, pp. 1–98, doi:10.1016/S0081-1947(08)60551-2.

[63] M. Khafizov, J. Pakarinen, L. He, D.H. Hurley, Impact of irradiation induced dislocation loops on thermal conductivity in ceramics, J. Am. Ceram. Soc. 102 (12) (2019) 7533–7542, doi:10.1111/jace.16616.

[64] M. Khafizov, I.-W. Park, A. Chernatynskiy, L. He, J. Lin, J.J. Moore, D. Swank, T. Lillo, S.R. Phillpot, A. El-Azab, D.H. Hurley, Thermal conductivity in nanocrystalline ceria thin films, J. Am. Ceram. Soc. 97 (2) (2014) 562–569, doi:10.1111/jace.12673.

[65] K. Bawane, X. Liu, T. Yao, M. Khafizov, A. French, J.M. Mann, L. Shao, J. Gan, D.H. Hurley, L. He, TEM characterization of dislocation loops in proton irradiated single crystal ThO_2, J. Nucl. Mater. 552 (2021) 152998, doi:10.1016/j.jnucmat.2021.152998. Accepted

[66] K.H. Lee, J.H. Crawford, Luminescence of the *F* center in sapphire, Phys. Rev. B 19 (1979) 3217–3221, doi:10.1103/PhysRevB.19.3217.

[67] B.D. Evans, G.J. Pogatshnik, Y. Chen, Optical properties of lattice defects in α-Al_2O_3, Nucl. Instrum. Meth. Phys. Res. B 91 (1) (1994) 258–262, doi:10.1016/0168-583X(94)96227-8.

[68] B.G. Childs, P.J. Harvey, J.B. Hallett, Optical absorption spectroscopy of ThO_2, J. Am. Ceram. Soc. 55 (11) (1972) 544–547, doi:10.1111/j.1151-2916.1972.tb13433.x.

[69] T.R. Griffiths, J. Dixon, Fast neutron radiation on single-crystal thorium dioxide. an optical absorption spectroscopy study of the f^0colour centre, J. Chem. Soc., Faraday Trans. 88 (1992) 3475–3482, doi:10.1039/FT9928803475.

[70] M.F. Riyad, V. Chauhan, M. Khafizov, Implementation of a multilayer model for measurement of thermal conductivity in ion beam irradiated samples using a modulated thermoreflectance approach, J. Nucl. Mater. 509 (2018) 134–144, doi:10.1016/j.jnucmat.2018.06.013.

[71] Z. Hua, A. Fleming, H. Ban, The study of using a multi-layered model to extract thermal property profiles of ion-irradiated materials, Int. J. Heat Mass Transf. 131 (2019) 206–216, doi:10.1016/j.ijheatmasstransfer.2018.11.056.

[72] V.S. Chauhan, J. Pakarinen, T. Yao, L. He, D.H. Hurley, M. Khafizov, Indirect characterization of point defects in proton irradiated ceria, Materialia 15 (2021) 101019, doi:10.1016/j.mtla.2021.101019.

[73] L. He, M. Khafizov, C. Jiang, B. Tyburska-Pschel, B.J. Jaques, P. Xiu, P. Xu, M.K. Meyer, K. Sridharan, D.P. Butt, J. Gan, Phase and defect evolution in uranium-nitrogen-oxygen system under irradiation, Acta Mater. 208 (2021) 116778, doi:10.1016/j.actamat.2021.116778.

[74] H.Y. Xiao, Y. Zhang, W.J. Weber, Trapping and diffusion of fission products in ThO_2 and CeO_2, J. Nucl. Mater. 414 (3) (2011) 464–470, doi:10.1016/j.jnucmat.2011.05.037.

[75] H.Y. Xiao, W.J. Weber, Oxygen vacancy formation and migration in $Ce_xTh_{1x}O_2$ solid solution, J. Phys. Chem. B 115 (20) (2011) 6524–6533, doi:10.1021/jp202016s.

[76] H.Y. Xiao, Y. Zhang, W.J. Weber, Stability and migration of charged oxygen interstitials in ThO_2 and CeO_2, Acta Mater. 61 (2013) 7639–7645.

[77] C. Onofri, C. Sabathier, C. Baumier, C. Bachelet, H. Palancher, M. Legros, Evolution of extended defects in polycrystalline Au-irradiated UO_2 using in situ TEM: temperature and fluence effects, J. Nucl. Mater. 482 (2016) 105–113, doi:10.1016/j.jnucmat.2016.10.011.
[78] D.A. Andersson, M.R. Tonks, L. Casillas, S. Vyas, P. Nerikar, B.P. Uberuaga, C.R. Stanek, Multiscale simulation of xenon diffusion and grain boundary segregation in UO_2, J. Nucl. Mater. 462 (2015) 15–25, doi:10.1016/j.jnucmat.2015.03.019.
[79] S.P. Waldow, R.A.D. Souza, Is excess faster than deficient? amolecular-dynamics study of oxygen-interstitial and oxygen-vacancy diffusion in CeO_2, J. Phys. Energy 2 (2) (2020) 024001, doi:10.1088/2515-7655/ab5cfd.
[80] S. Khalil, T. Allen, A. El-Azab, Off-stoichiometric defect clustering in irradiated oxides, Chem. Phys. 487 (2017) 1–10, doi:10.1016/j.chemphys.2017.01.014.
[81] A.I. Popov, E.A. Kotomin, J. Maier, Basic properties of the F-type centers in halides, oxides and perovskites, Nucl. Instrum. Meth. Phys. Res. B 268 (19) (2010) 3084–3089, doi:10.1016/j.nimb.2010.05.053.
[82] G.P. Pells, Radiation damage effects in alumina, J. Am. Ceram. Soc. 77 (2) (1994) 368–377, doi:10.1111/j.1151-2916.1994.tb07004.x.
[83] M. Jin, C. Jiang, J. Gan, D.H. Hurley, Systematic analysis on the primary radiation damage in $Th_{1-x}U_xO_2$ fluorite systems, J. Nucl. Mater. 536 (2020) 152144, doi:10.1016/j.jnucmat.2020.152144.
[84] C. Matthews, R. Perriot, M.W.D. Cooper, C.R. Stanek, D.A. Andersson, Cluster dynamics simulation of uranium self-diffusion during irradiation in UO_2, J. Nucl. Mater. 527 (2019) 151787, doi:10.1016/j.jnucmat.2019.151787.
[85] C.T. Walker, Thermal conductivity of some alkali halides containing *F* centers, Phys. Rev. 132 (1963) 1963–1975, doi:10.1103/PhysRev.132.1963.